



Microstructure and thermal properties of inflight rare-earth doped thermal barriers prepared by suspension plasma spray

Stephanie Gong^a, Kent VanEvery^b, Hsin Wang^c, Rodney W. Trice^{a,*}

^a School of Materials Engineering, Purdue University, Neil Armstrong Hall of Engineering, 701 West Stadium Avenue, West Lafayette, IN 47907, USA

^b Progressive Surface, 4695 Danvers Dr. SE, Grand Rapids, MI 49512, USA

^c High Temperature Materials Laboratory, Oak Ridge National Laboratory, Building 4515, 1 Bethel Valley Rd, Oak Ridge, TN 37831, USA

Received 21 August 2013; received in revised form 6 November 2013; accepted 12 November 2013

Available online 6 December 2013

Abstract

Rare-earth doped yttria-stabilized zirconia (YSZ) coatings with lower thermal conductivity have been fabricated via suspension plasma spray by dissolving rare-earth nitrates into YSZ powder-ethanol suspensions prior to plasma spraying. The effect of dopant concentration and dopant type on properties of the coatings was determined by comparing two coatings containing different concentrations of the same dopant pair ($\text{Nd}_2\text{O}_3/\text{Yb}_2\text{O}_3$), and three coatings having similar concentrations of different dopant pairs ($\text{Nd}_2\text{O}_3/\text{Yb}_2\text{O}_3$, $\text{Nd}_2\text{O}_3/\text{Gd}_2\text{O}_3$, and $\text{Gd}_2\text{O}_3/\text{Yb}_2\text{O}_3$). The porosity content of the coating was found to increase with increased total rare-earth dopant concentration but did not significantly change with dopant pairs. The cross-sectional morphology of every coating displayed a cauliflower-like structure. However, the most heavily doped coating exhibited a larger surface roughness and feathery features in the columnar structures. The thermal conductivity measurement showed that the thermal conductivity decreased with increased $\text{Nd}_2\text{O}_3/\text{Yb}_2\text{O}_3$ concentration. Among coatings containing different dopant pairs, the $\text{Gd}_2\text{O}_3/\text{Yb}_2\text{O}_3$ doped coating exhibited lowest conductivity.

© 2013 Elsevier Ltd. All rights reserved.

Keywords: Thermal barrier coatings; Suspension plasma spray; Rare-earth oxides

1. Introduction

Thermal barrier coatings (TBCs) are essential components of gas turbine engines used in commercial aircraft and power generation. These ceramic coatings, ranging from 100 to 500 μm in thickness, help maintain the integrity of the underlying engine components by reducing the heat flux reaching these components.¹ Consequently, TBCs can be used to reduce the cooling air required to maintain safe engine component temperatures during operation and/or increase the gas temperature in the engine, both of which increase the engine efficiency.² Commercial TBCs are currently 4–4.5 mol.% (7–8 wt.%) yttria-stabilized zirconia (YSZ) coatings produced by air plasma spray (APS) or electron beam physical vapor deposition (EB-PVD). YSZ has been chosen based on its relatively low thermal conductivity, high thermal expansion coefficient, and long lifetime

compared to other ceramics.³ Although YSZ has many favorable properties, sintering and phase decomposition occurring in this material above 1200 °C are detrimental to thermal barriers. Since the gas temperatures of existing turbines exceed 1200 °C, YSZ TBCs are not well suited for the next generation of gas turbines that are designed to operate at even higher temperatures.^{4–6}

Various approaches have been attempted to improve the current TBCs.⁷ Among these efforts, coatings produced by the defect clustering technique of Zhu and Miller^{8–11} were shown to be promising. In their study, the largest decrease in thermal conductivity from the baseline YSZ coatings occurred when doping an equal molar ratio of paired rare-earth (RE) oxides.^{10,11} The dopant pair was chosen such that one dopant has a larger ionic size and the other has a smaller ionic size relative to that of the stabilizing yttrium.⁹ Both high resolution transmission electron microscopy images and compositional maps obtained by electron energy loss spectroscopy of these doped coatings revealed the segregation of rare-earth oxides in the zirconia matrix as nanometer-sized clusters.¹¹ It was proposed that these defects scatter phonons, lowering the thermal conductivity of

* Corresponding author. Tel.: +1 765 4946405; fax: +1 765 4941204.
E-mail address: rtrice@purdue.edu (R.W. Trice).

Table 1
Designed test matrix to study the effect of rare-earth dopants on SPS coatings.

Type/nominal concentration	Y ₂ O ₃ (mol.%)	Nd ₂ O ₃ (mol.%)	Yb ₂ O ₃ (mol.%)	Gd ₂ O ₃ (mol.%)	RE dopant ratio	Total dopant concentration (mol.%)	Total stabilizer (mol.%)
Baseline	4.5	–	–	–	–	–	4.5
Nd ₂ O ₃ /Yb ₂ O ₃	3.8	8.68	7.42	–	0.85	16.1	19.9
Nd ₂ O ₃ /Yb ₂ O ₃	4.3	2.39	2.05	–	0.86	4.4	8.74
Nd ₂ O ₃ /Gd ₂ O ₃	4.3	2.39	–	2.26	0.95	4.7	8.95
Gd ₂ O ₃ /Yb ₂ O ₃	4.3	–	2.05	2.27	0.90	4.3	8.62

Table 2
Ionic radii of the matrix and rare-earth elements present in the SPS coatings.¹⁷

Element	Zr ⁴⁺	Yb ³⁺	Y ³⁺	Gd ³⁺	Nd ³⁺
Ionic radius (pm)	84	98	102	106	112

the coating. In addition, based on the rate of increase in thermal conductivity measured at 1316 °C, these rare-earth doped coatings were found to be more sintering resistant than the YSZ coating.¹⁰

The rare-earth doped coatings examined by Zhu and Miller^{10,11} were fabricated via APS and EB-PVD. For the APS coatings, powder agglomerates of YSZ and the desired dopants were spray dried to form powders that could be easily flowed into the plasma plume.^{10,11} Another process that could be used to synthesize nanometer-sized oxide particles and coatings of varying compositions is solution (liquid) precursor spray.^{12–14} In this process, a solution containing precursor salts or organics is injected into the plasma to form oxide materials through pyrolysis. In the present study, suspension plasma spray (SPS) was employed to produce the rare-earth doped YSZ coatings. Different from the abovementioned processes, the starting feedstock of SPS is a colloidal solution of nanometer-sized YSZ powders. Dopants were added by dissolving rare-earth nitrates into the YSZ suspension, followed by plasma spraying. Using this method, VanEvery et al.¹⁵ produced a Nd₂O₃/Yb₂O₃ doped YSZ coating, demonstrating the feasibility of using SPS to incorporate dopants. This relatively new fabrication method offers the ability to spray nanometer-sized powders and to tailor the coating composition easily without having to make large batches of spray-dried powders.^{15,16} In this work, a total of four rare-earth doped coatings that have different compositions and a baseline 4.5 mol.% YSZ coating were produced and characterized to study the effect of increasing dopant concentration and changing dopant pair type on the properties of the coatings.

2. Experimental procedure

2.1. Suspension compositions

Table 1 shows the compositions chosen to study the effects of rare-earth dopants on SPS YSZ coatings. Three rare-earth dopant pairs were selected based on the ionic radii data presented in Table 2.¹⁷ The first two dopant pairs, Nd₂O₃/Yb₂O₃ and Gd₂O₃/Yb₂O₃, are composed of one larger ion (Nd³⁺ or Gd³⁺) and one smaller ion (Yb³⁺) relative to the primary

stabilizer, Y³⁺. The size difference between the two dopant cations is greater for the Nd₂O₃/Yb₂O₃ pair than the Gd₂O₃/Yb₂O₃ pair. Conversely, the third dopant pair, Gd₂O₃/Nd₂O₃, consists of two larger dopant cations compared to the Y³⁺. All three coatings contained nominally 4.3–4.7 mol.% added dopants. Furthermore, two concentrations of Nd₂O₃/Yb₂O₃ dopants (4.4 and 16.1 mol.%) were investigated.

The dopant molar ratios of the suspensions produced in this study varied from 0.85 to 0.95, with a ratio of 1 being ideal.⁹ Furthermore, the suspension compositions listed in Table 1 were presented under the assumption that all rare-earth ions existing in the solvent would be incorporated into the coatings. The amount of dopant actually incorporated into a coating is expected to be less than the designed values due to losses during spraying.¹⁵ The actual coating compositions have been determined and are provided in Section 3.

2.2. Preparation and characterization of suspensions

Each suspension prepared contained 20 wt.% of 4.5 mol.% YSZ powder (Item 464228, Sigma–Aldrich, St. Louis, MO). The starting feedstock was received as loose agglomerates that were primarily composed of powders ranging from 80 to 150 nm in diameter. Ethanol was chosen as the solvent for the suspension due to lower heat of evaporation compared to water.^{18,19} Wet milling was used to break apart the YSZ agglomerates, and 1 wt.% of phosphate ester dispersant (Triton QS-44, Sigma–Aldrich, St. Louis, MO) was added prior to the milling.¹⁵

To prepare suspensions for the rare-earth doped coatings, two of the following hydrated nitrates, Gd(NO₃)₃·6H₂O, Nd(NO₃)₃·6H₂O, or Yb(NO₃)₃·5H₂O, were added to the suspensions prior to milling. Wet milling of each suspension was performed at ~140 rpm for 8 h and stored until use. The number based d₅₀ of the baseline suspension and most doped suspension after milling were found to be 747 ± 60 and 727 ± 11 nm, respectively, indicating that the powders were slightly agglomerated. Prior to spraying, the suspensions were put in an ultrasonic bath for approximately 15 min and poured through a 25 or 180 μm sieve to breakup and remove any significantly large agglomerates that could cause clogging.

Thermogravimetric analysis (TGA) was performed on the baseline and the most heavily doped suspensions to measure their evaporation rate as weight loss with respect to time. The suspensions were heated at 20 °C/min to a temperature between

56 and 57.5 °C. The TGA furnace temperature dropped a few degrees as the liquid evaporated. The data was recorded until the liquid was fully evaporated.

2.3. Fabrication of the SPS coatings

Coatings were fabricated at Progressive Surface (Grand Rapids, MI) using a 100HE plasma spray torch. Suspensions were injected externally through a 229 μm orifice into the plasma via a Progressive LiquifeederHE which controlled the flow rate at 47 ± 1.5 ml/min. A power of 105 kW and plasma gas flows of 85 slm Ar, 57 slm N₂, and 57 slm H₂ were used for all runs. Each suspension was sprayed onto a 75 by 75 mm copper substrate that had been previously grit blasted to enhance coating adherence. A standoff distance of 7 cm was used.

Prior to the injection of suspension, the substrates were preheated to 370 °C by rastering the plasma spray gun across the surface. During the coating process, the temperature of the substrate eventually reached a steady value of ~ 480 °C. These temperatures were determined using a thermocouple that was inserted into a substrate during a test run. To prevent spallation of the coatings, cooling air was used during spraying to reduce the thermally generated stresses within the coating. Compressed air was directed onto the back of the substrate at a flow rate of 0.028 m³/s, and an air nozzle attached below the plasma gun cooled the coating surface during spraying. The spray parameters were kept approximately constant for each run, and the conditions were not optimized. Prior to evaluation, coatings were removed from the substrates by soaking in nitric acid. Hydrochloric acid was then used to dissolve any copper oxide formed between the coating-substrate interface during spraying. Energy-dispersive X-ray spectroscopy was used to confirm the absence of copper on back of the coating before characterization.

2.4. Phase and microstructural analysis of the coatings

The crystal structures of the as-sprayed coatings were examined using CuK α X-ray diffraction (XRD) (Bruker D8 diffractometer, Billerica, MA). XRD was also used to study as-received powders and selected suspensions which were drop cast on glass substrates and then dried on a heated plate. XRD scans from 20° to 80° 2 θ , which were obtained at a scan rate of $\sim 5^\circ/\text{min}$ at an increment of 0.02°, were examined to detect monoclinic-ZrO₂ (*m*-ZrO₂) or other phases in the as-sprayed coatings. Additionally, XRD scans ranging from 2 θ of 72° to 76° were acquired using a slower scan rate of $\sim 1^\circ/\text{min}$ at an increment of 0.0014° to improve the identification of peaks associated with non-transformable tetragonal (*t'*-ZrO₂), equilibrium tetragonal (*t*-ZrO₂), or cubic (*c*-ZrO₂) phases.²⁰

Microstructural features of the coatings were characterized by scanning electron microscopy (SEM) (Phillips XL40 Schottky FEG and FEI Quanta 3D Schottky FEG, Hillsboro, OR). Surfaces and fractured cross-sections of the coatings were examined. Coating cross section samples were also polished and thermally etched at 1100 °C for one hour to manifest the grain boundaries.²¹

2.5. Thermal conductivity measurements

The thermal conductivity of the coating was calculated by multiplying diffusivity (cm²/s) times the heat capacity (J/g/°C) and bulk density (g/cm³). This value was multiplied by 100 for final thermal conductivity values of W/m/K.⁵ The thermal diffusivity values were measured at Oak Ridge National Laboratory-High Temperature Materials Laboratory (HTML) using the laser flash method. Measurements were taken at increments of 100 °C from a temperature of 100–1200 °C. A thin layer of colloidal graphite was sprayed onto both sides of the coating before the measurement to enhance the absorption of the applied energy.²² For each coating composition, at least two specimens were tested. The tested specimens were disks with diameters of ~ 12.5 mm. Sample thicknesses were measured using SEM images of the fractured surface of tested samples. The coating thickness was then determined by performing a thickness measurement every 50 μm over at least a 1 mm length. By imaging a standard sample (SEM Low Mag. Calibration Ruler, Ted Pella Inc., Redding, CA) at the same magnification, the scale bar was found to be accurate within 2% of the length. The specific heat of the rare-earth doped coatings was not measured. Instead, the specific heat of 4.5 mol.% YSZ provided in ref. ²³ was used to determine the thermal conductivity of all coatings. Therefore, the thermal conductivity results do not reflect the change, if any, in specific heat upon doping of YSZ. The bulk density, which includes both open and closed porosity, of the specimens used to compute the thermal conductivity was measured by the Archimedes method.²⁴

2.6. Determination of theoretical density

The theoretical density, representing a fully dense coating, for each coating composition was obtained by dividing the total mass of atoms in a unit cell by the unit cell volume. By determining the actual composition of the coating, the number of each atom type in a single unit cell was calculated and then converted to mass. The oxygen vacancy concentration induced by the trivalent stabilizers was also calculated for each coating type and included in the theoretical density. Lattice parameters for determining the unit cell volume were obtained by computing the interplanar distance of the {400} planes from the XRD results. The crystal structures of the cubic and tetragonal zirconia were considered as the cubic fluorite and deformed fluorite structure with oxygen atoms displacing from their ideal positions, respectively.^{25,26} However, as it will be discussed later, the fraction of each phase in the rare-earth doped zirconia was not lucid due to overlapping peaks in the XRD patterns. Nevertheless, this also indicates that the interplanar distances are not that different, and therefore the unit cell volumes should be similar regardless of crystal structure. This is confirmed when the theoretical densities for different scenarios (e.g. single tetragonal phase, 50% tetragonal with 50% cubic phase, and two cubic phases) of each doped coating were calculated and were found to vary within 0.02 g/cm³. The reported value is the average of the density values calculated for the scenarios described above. Lastly, the total

Table 3
Compositions of the coatings and the corresponding bulk density and theoretical density.

Sample	Y ₂ O ₃ (mol.%)	Nd ₂ O ₃ (mol.%)	Yb ₂ O ₃ (mol.%)	Gd ₂ O ₃ (mol.%)	Total stabilizer (mol.%)	RE dopant ratio	Bulk density (g/cm ³)	Theoretical density (g/cm ³)	Total porosity (vol. %)
Baseline	4.50	–	–	–	4.5	–	4.37 ± 0.19	6.08 ± 0.01	28 ± 3
Nd ₂ O ₃ /Yb ₂ O ₃	4.20	5.65	5.32	0.00	15.2	0.94	3.50 ± 0.18	6.50 ± 0.01	46 ± 3
Nd ₂ O ₃ /Yb ₂ O ₃	4.66	1.50	1.28	0.00	7.4	0.85	4.08 ± 0.15	6.21 ± 0.02	34 ± 3
Nd ₂ O ₃ /Gd ₂ O ₃	4.55	1.53	0.03	1.85	8.0	0.83	3.77 ± 0.10	6.20 ± 0.02	39 ± 2
Gd ₂ O ₃ /Yb ₂ O ₃	4.44	0.04	1.17	1.71	7.4	0.68	3.96 ± 0.09	6.25 ± 0.02	37 ± 2

porosity, which is determined by $[1 - \text{bulk density}/\text{theoretical density}] \times 100\%$, is reported.

3. Results and discussion

3.1. Coating compositions and physical properties

Table 3 shows the actual compositions of the baseline and rare-earth doped coatings fabricated presently. These coatings also contained 1.1–1.2 mol.% of HfO₂, which are not shown in the table. Except for the composition of the baseline coating, which was provided by the manufacturer, compositions of the doped coatings were measured using inductively coupled plasma techniques (NSL Analytical Inc., Cleveland, OH). With reference to Table 1, an average of $68 \pm 8\%$ of the rare-earth ions added to the suspension in the form of nitrates was incorporated into the sprayed coatings. For example, spraying a suspension that contained 32.2 mol.% of Nd³⁺ and Yb³⁺ resulted in a coating that has 10.9 mol.% of (Nd, Yb)₂O₃ instead of 16.1 mol.% (Nd, Yb)₂O₃. Furthermore, the efficiency to dope rare-earth oxides was found to depend on the dopant type. A higher percentage of Gd³⁺ was integrated into the coatings compared to Nd³⁺ and Yb³⁺. Since the ionic radius of Gd³⁺ lies between that of the Nd³⁺ and Yb³⁺, differences in dopant incorporation were unlikely due to different atomic diffusion rates which can be related to the dopant size. Further investigation is needed to determine the cause of these results. Due to differences in dopant incorporation efficiency, the measured dopant ratio deviated from the designed dopant ratio, ideally 1 as determined by Zhu and Miller work^{10,11}, and was found to vary from 0.68 to 0.94.

The bulk density, theoretical density, and the total porosity of the as-sprayed coatings are shown in Table 3. The reported bulk density is an average density of at least seven individual coating specimens. It was found that the 7.4 mol.% (Y, Nd, Yb)₂O₃-ZrO₂ and 15.2 mol.% (Y, Nd, Yb)₂O₃-ZrO₂ coatings contained 6 and 18 vol.% more porosity, respectively, than the baseline coating. This finding indicated that the porosity content of the coating increased with total dopant concentration. Conversely, while the 7.4 mol.% (Y, Nd, Yb)₂O₃-ZrO₂ coating was slightly denser than the other two 7–8 mol.% doped coatings, the effect of dopant pair type on porosity was not as significant as increasing the dopant concentration.

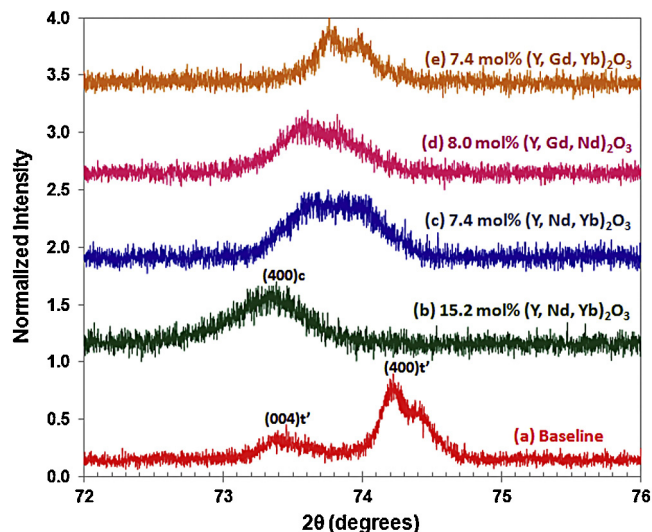


Fig. 1. X-ray diffraction plots for various coatings. The shift of {400} peaks toward smaller 2θ values is an indication of lattice expansion induced by rare-earth doping. The tetragonal split observed in the baseline coating also became less pronounced in the doped coatings.

3.2. Phase analysis of the powders and as-sprayed coatings

XRD of as-received powders: The XRD patterns (not shown) of the as-received YSZ powders and drop-cast films of the baseline and most heavily doped suspension were the same, indicating that the incorporation of rare-earth dopants into YSZ powders was not accomplished by mechanical alloying during ball milling. Low intensity peaks at 28.5° and 31.5° were observed in these scans, which demonstrated the presence of *m*-ZrO₂ in the as-received powders.

Effect of rare-earth on coating phase assemblage: The XRD results from 20° to 80° (not shown) for all of the as-sprayed coatings revealed no peaks other than those attributable to tetragonal or cubic zirconia. Specifically, no RE₂O₃ or *m*-ZrO₂ peaks were noted in the scans. Spectra focused on the {400} peaks located in the 72° – 76° regime are shown in Fig. 1, with a summary of the 7–8 mol.% rare-earth doped results in Fig. 2. In agreement with the published data, the baseline coating consisted of peaks at $\sim 73.4^\circ$ and $\sim 74.2^\circ$ that are corresponding to (004) and (400) peaks of the *t'*-ZrO₂ phase.²⁰ The *t'* phase emerges as molten droplets impinged onto the substrate and rapidly solidified. The short solidification time impedes yttrium diffusion, leaving the zirconia supersaturated with yttrium

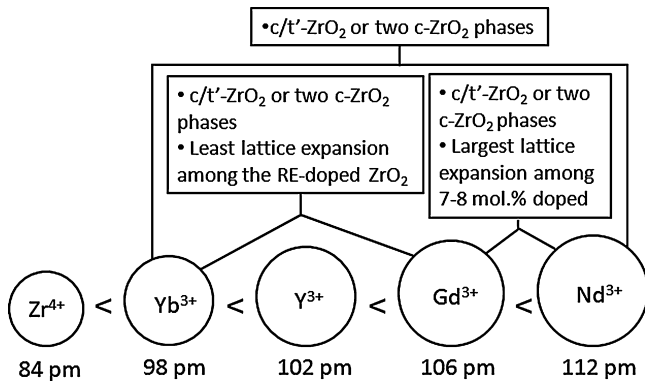


Fig. 2. Summary of the phase assemblage results for the as-sprayed coatings from Fig. 1 for the 7–8 mol.% rare-earth doped coatings with respect to the dopant size.¹⁷

(*t'*-ZrO₂). A small amount of *t*-ZrO₂ may be present in the baseline coating, as a shoulder peak was observed at $\sim 74.4^\circ$. However, the CuK α_2 line of the main peak also lies at the same 2θ value, and therefore can also contribute to the intensity of this shoulder peak.

In the case of 15.2 mol.% (Y, Nd, Yb)₂O₃-ZrO₂ coating, one broad peak was observed at $\sim 73.3^\circ$, suggesting the formation of cubic phase. In contrast, the XRD pattern for the coating containing 7.4 mol.% of (Y, Nd, Yb)₂O₃-ZrO₂ displayed overlapping peaks. It is unlikely that the overlapping peaks observed in this study correspond to a single tetragonal structure. The inference is that the intensity ratio of the two peaks, instead of being 1:2 which is the case for the split tetragonal peaks, is ~ 1 . Similar to the previous case, both the 8 mol.% (Y, Nd, Gd)₂O₃-ZrO₂ and 7.4 mol.% (Y, Gd, Yb)₂O₃-ZrO₂ coatings exhibited overlapping peaks. It is suspected that the overlapping peaks arise from the existence of more than one phase, possibly a combination of cubic and tetragonal phases or two cubic phases.

Two mechanisms by which more than one phase can form are proposed. Zhu and Miller²⁷ reported that rare-earth doped YSZ coatings with 6 mol.% or less of stabilizer concentration had a predominantly tetragonal phase while coatings with 10 mol.% or more of stabilizer had a cubic phase. Therefore, a stabilizer concentration of 7–8 mol.% is likely lying on the boundary between tetragonal to cubic formation. Long range diffusion may be limited by the short resident time of powders in the plume and causes non-uniform distribution of the dopant atoms. Regions with higher dopant concentration thus can be stabilized into cubic structure, while the regions with less dopant concentration can form tetragonal zirconia. The above mechanism assumes only short range diffusion; however, another possibility is that the atomic diffusion is rapid enough to achieve long range diffusion. In this case, each atom type can migrate to their preferred sites and lead to the formation of preferred lattice spacings.¹⁵ This is supported by the observation of Zhu and Miller¹¹ that rare-earth dopants can segregate independently, causing regions of the coating rich in different types of dopant atoms. Note that the Zhu and Miller coatings, prior to their characterization, have been heat treated where long range diffusion can occur.¹¹ This preferential segregation can also lead to the

formation of different phases, as the phase stability of zirconia is dependent on the ionic radius of the stabilizer atom, which was evident in a singly rare-earth doped zirconia system.¹⁷

The addition of the rare-earth dopants expanded the zirconia lattice. It is evident from Fig. 1 that the (4 0 0) peaks of the cubic and/or tetragonal phase present in the doped coatings were shifted to a lower 2θ value relative to the (4 0 0) *t'*-ZrO₂ peak of the baseline coating. More peak shifting was observed for the 15.2 mol.% (Y, Nd, Yb)₂O₃-ZrO₂ coating than the 7.4 mol.% (Y, Nd, Yb)₂O₃-ZrO₂ coating, indicating that the interplanar spacing and hence the lattice constant, *a*, had increased with dopant concentration. This result is consistent with the findings of Zhu and Miller.¹¹ The extent of the expansion also depended on the dopant type. The coating containing the two larger dopants (Gd³⁺ and Nd³⁺) had the largest average lattice constant, whereas the coating containing the smaller dopants (Gd³⁺ and Yb³⁺) had the smallest lattices among the 7–8 mol.% doped coatings.

3.3. Microstructures of the as-sprayed coatings

Characterization of the coating surface microstructure: Fig. 3 shows the top surfaces of the baseline and doped coatings. It was observed that all coatings, with or without rare-earth dopants, displayed a cauliflower-like structure, which was formed by the tops of the columnar structures that comprised the coating. Despite using the same spray parameters, the porosity between the columns (inter-columnar porosity) illustrated by the white arrow in Fig. 3(a), was observed to increase with increased Nd₂O₃/Yb₂O₃ concentration (Fig. 3(a–c)). In contrast, as evident from Fig. 3(b–e), there was no significant change in the microstructure of coatings containing different dopant pairs but similar concentration. These observations are consistent with the porosity data shown in Table 3.

Characterization of the coating cross-sectional microstructure: A clearer view of the columnar structures of the coatings is provided in Fig. 4. From the polished cross-sections, it was observed that the microstructures of the baseline and the 7.4 mol.% (Y, Nd, Yb)₂O₃-ZrO₂ coatings were similar, although more inter-columnar porosity, separating each column into sub-columns, was seen in the latter one. In comparison, the 15.2 mol.% (Y, Nd, Yb)₂O₃-ZrO₂ coating exhibited a larger surface roughness and much wider inter-columnar pores, especially near the top of the coating. Furthermore, the periphery of each column displayed a feathery structure, which was not as pronounced in the baseline and 7.4 mol.% (Y, Nd, Yb)₂O₃-ZrO₂ coating.

It is interesting to note that these SPS coatings have similar microstructural features to EB-PVD coatings. Both exhibit columnar structures and feathery features, but those in SPS coatings studied presently were at least one order of magnitude larger in size.²⁸ Although the mechanical properties of the SPS coatings were not measured, the existence of inter-columnar porosity is expected to improve coating compliance similar to the gaps between columns in EB-PVD coatings.²⁹ However, too much porosity can significantly reduce the mechanical integrity of the coatings and would have to be investigated.³⁰

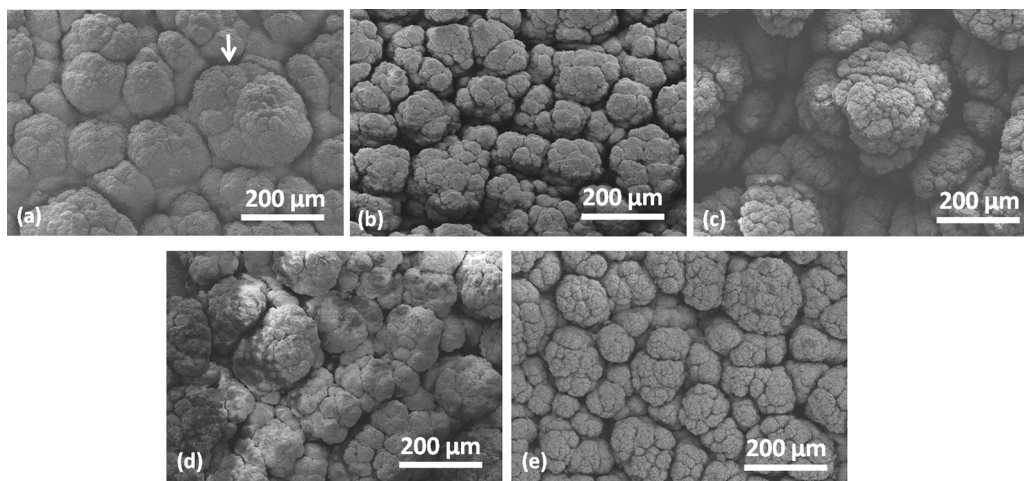


Fig. 3. SEM images showing the top surfaces of (a) baseline, (b) 7.4 mol.% (Y, Nd, Yb)₂O₃, (c) 15.2 mol.% (Y, Nd, Yb)₂O₃, (d) 8.0 mol.% (Y, Nd, Gd)₂O₃, and (e) 7.4 mol.% (Y, Gd, Yb)₂O₃-doped coatings. The fraction of inter-columnar porosity, indicated by the white arrow in (a), was found to increase with dopant amount.

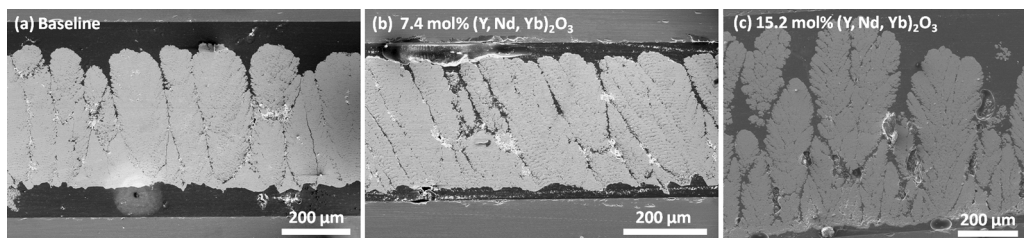


Fig. 4. Polished cross-sectional surfaces of (a) baseline, (b) 7.4 mol.% (Y, Nd, Yb)₂O₃, and (c) 15.2 mol.% (Y, Nd, Yb)₂O₃ doped coatings. The 15.2 mol.% (Y, Nd, Yb)₂O₃ not only is more porous but also exhibits a feathery like microstructure that is not as obvious in other coatings.

Columnar structures have also been observed in other SPS coatings.^{31,32} As proposed by VanEvery et al.,³² the columns are formed when the powder droplets are deposited on the sides of surface humps present on the substrates. This process occurs when the droplets are small enough to be affected by the plasma flow. Thus, the columnar structures tend to be readily observed in SPS coatings sprayed with sub-micrometer or nanometer-sized powders, and the aspects for these structures, such as the cauliflower-like top surface, become less distinct with increasing droplet size, as can result from using suspensions that contain higher powder loadings.³² While it is difficult to characterize the size of the droplets that formed the coatings in this study, the microstructures suggest rare-earth nitrate concentration in the suspension may have an effect on the size of droplets formed in the plasma plume.

Another microstructural feature appearing in all coatings was the inter-pass boundaries (IPB), which were apparent in the cross-sectional view of the coatings. These boundaries have been found in both SPS and solution precursor plasma spray (SPPS) coatings.^{33,34} Fauchais et al.³⁴ explained the formation of IPB as a result of depositing overspray powders, which are partially melted or resolidified powders that have traveled through the fringes of the plume. Example of such a feature observed in the baseline coating is shown in Fig. 5. The polished coating shown in Fig. 5(b and c) was further heat treated at 1100 °C for 1 h to reveal grain boundaries and pores which were embedded within the coatings. As seen in these two images, the columnar

structure described above was composed of relatively dense coating layers separating by numerous IPBs. Each boundary was associated with one spray pass. A closer examination of the boundaries (Fig. 5(c)) revealed the presence of spherical particles, indicating that the boundaries were consist of partially melted or resolidified powders. This observation is consistent with the findings of other studies.^{33,34}

The amount of overspray powders was found to increase with rare-earth doping. Fig. 6 shows the top views of the baseline and 15.2 mol.% (Y, Nd, Yb)₂O₃ coating. It can be seen from Fig. 6(a) that the top of one column in the baseline coating was covered with stacks of micrometer-sized lamella, which formed upon the impact of molten powders with the coating. Further zoom in on the top surface showed the presence of overspray powders (Fig. 6(b)). In comparison, the 15.2 mol.% (Y, Nd, Yb)₂O₃ coating had so many more partially and resolidified powders throughout the top surface that the underlying lamellae were fully covered (Fig. 6(c and d)). The origin of these overspray powders observed on the top surface was the same as the ones that generate the IPBs. This result demonstrates that alloying rare-earth dopants can produce a more porous coating by incorporating more overspray powders, which cannot make complete contact with each other and leaves voids in between. It should be recalled that the XRD patterns for the doped coatings on Fig. 1 showed different peak shapes and locations than the 4.5 mol.% YSZ, implying that the dopant ions have diffused into and distorted the YSZ lattice.

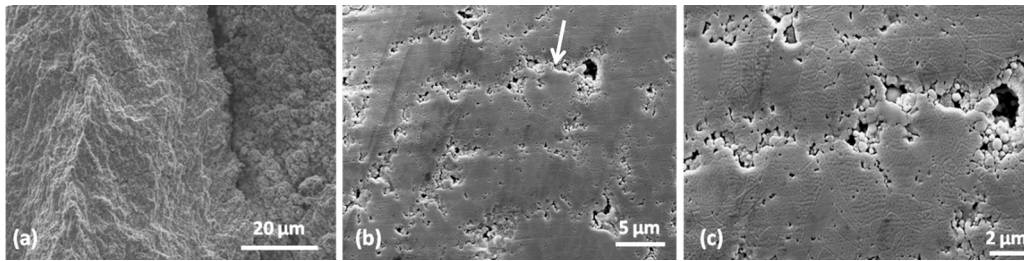


Fig. 5. Cross-section images of baseline coatings showing inter-pass boundaries at different magnifications. Coating shown in (b and c) has been heat treated at 1100 °C for 1 h to reveal grain boundaries, intergranular and intragranular pores. An example of the boundary is indicated by the white arrow.

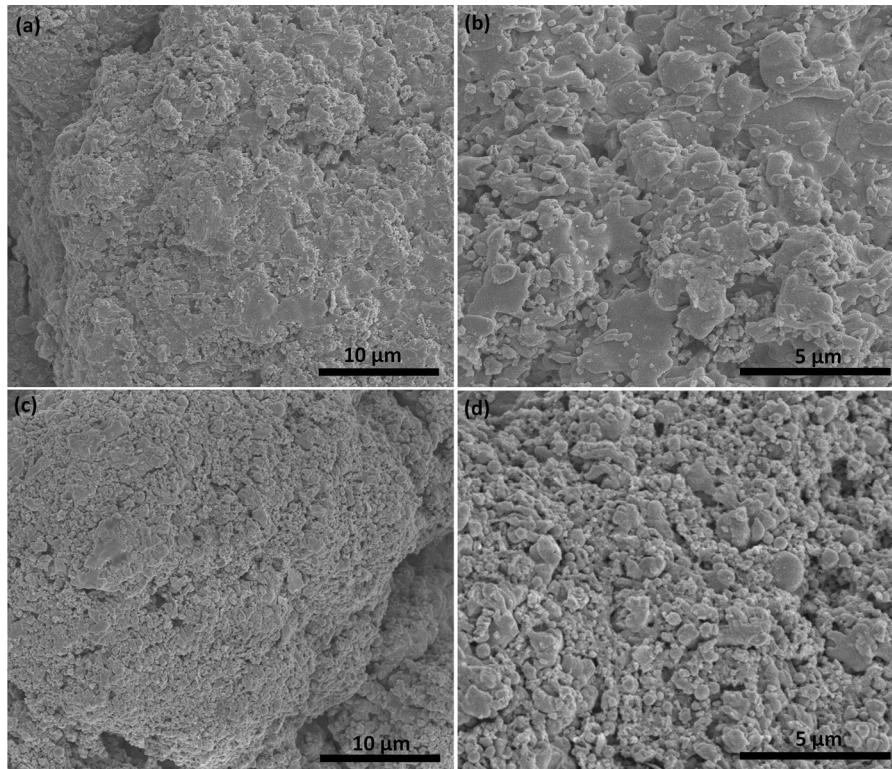


Fig. 6. Top surface of the baseline coating (a and b) and the 15.2 mol.% (Y, Nd, Yb)₂O₃-ZrO₂ coating (c and d). Comparison of the two coatings showed that more partially or resolidified powders were deposited on the doped coating, which induced porosity.

Effect of suspension characteristics on microstructure formation: The microstructure of SPS coatings have been found to depend on both the spraying parameters and suspension characteristics, but only the latter is considered in this work since the controllable spraying parameters were kept roughly constant.^{18,35,36} With a fixed powder loading, viscosity and surface tension are the suspension characteristics that can affect the microstructure by influencing the fragmentation of the injected stream, which is a process where the plasma flow breaks the stream into droplets.³⁶ Rampon et al.,³⁵ observed an 8% decrease in the coating porosity produced by a more viscous suspension (18 mPa s versus 6 mPa s). However, based on observation, the viscosities of the suspensions did not seem to decrease but increased upon the addition of rare-earth nitrates. This suggests that the increase in porosity with dopant concentration may be caused by other factors, such as the suspension surface tension.

Thermogravimetric analysis was performed to investigate further the effect of nitrate addition. The results showed that the suspension used to make the 15.2 mol.% (Y, Nd, Yb)₂O₃-ZrO₂ coating evaporated at a slower rate compared to the baseline suspension. Calculation of the water amount in one mole of the hydrated Nd- and Yb-nitrates used to create the 15.2 mol.% (Y, Nd, Yb)₂O₃-ZrO₂ coating indicated that 7 wt.% of additional water was in the suspension. The energy required to heat and evaporate 100 g of ethanol versus 93 g of ethanol with 7 g of water were calculated to be 97 kJ and 108 kJ, respectively.^{37,38} Consequently, the extra energy spent to evaporate water would have reduced the plasma enthalpy available for melting the powder, increasing the likelihood of partially melted particles in the coating. The heat produced by the combustion of ethanol was not included in this calculation since the oxygen available for combustion is likely to be small in the region of the plasma plume where powders were melting.

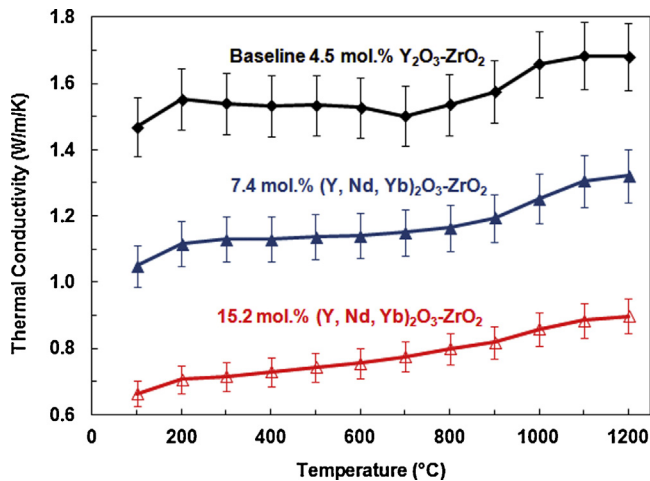


Fig. 7. Thermal conductivity of coatings containing different $\text{Nd}_2\text{O}_3/\text{Yb}_2\text{O}_3$ concentration as a function of testing temperature. The thermal conductivity is observed to decrease with increasing dopant concentration.

Table 4

The change in thermal conductivity in two temperature regimes (200–700 °C and 800–1000 °C) for the coatings investigated.

Sample	k_{th} change from 200 to 700 °C (W/m/K)	k_{th} change from 800 to 1000 °C (W/m/K)
Baseline	−0.05	0.12
15.2 mol.% (Y, Nd, Yb) ₂ O ₃	0.07	0.06
7.4 mol.% (Y, Nd, Yb) ₂ O ₃	0.03	0.09
8.0 mol.% (Y, Nd, Gd) ₂ O ₃	0.09	0.10
7.4 mol.% (Y, Gd, Yb) ₂ O ₃	0.01	0.08

3.4. Thermal conductivity of the as-sprayed coatings

Effect of dopant concentration on thermal conductivity: The microstructure of the SPS coatings, as demonstrated in Figs. 4 and 5, is anisotropic. Thus, the thermal conductivity of the coating should also be dependent on direction. In the current study, the thermal conductivity was measured through the thickness of the coating with the measurement error estimated to be $\pm 6\%$. Fig. 7 shows the thermal conductivity of the as-sprayed coatings containing different amounts of $\text{Nd}_2\text{O}_3/\text{Yb}_2\text{O}_3$ as a function of testing temperature. The incorporation of the dopants reduced the thermal conductivity at any given temperature, with the coating that had the highest dopant concentration being the least conductive.

Increasing dopant concentration also had an influence on the temperature dependence of thermal conductivity between 200 °C and 700 °C due to atomic defect scattering (Fig. 7). Table 4 presents the change in thermal conductivity in this temperature regime. The negative thermal conductivity change for the baseline coating indicated a slight decrease in conductivity with temperature and is consistent with the trend that was observed in zirconia coatings having a single tetragonal phase.³⁹

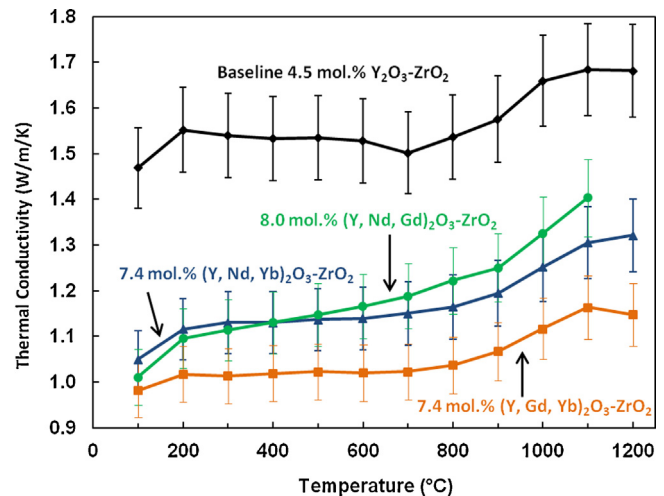


Fig. 8. An illustration on the effect of dopant pair type on thermal conductivity as a function of testing temperature.

In contrast, the slightly upward temperature dependence on the thermal conductivity of 7.4 mol.% (Y, Nd, Yb)₂O₃-ZrO₂ indicated the presence of both tetragonal and cubic phases or solely cubic phases.³⁹ Compared to those two, the 15.2 mol.% (Y, Nd, Yb)₂O₃-ZrO₂ coating showed the highest thermal conductivity increase, suggesting a higher degree of atomic ordering in the cubic phase. This is supported by the XRD spectra shown in Fig. 1.

As observed in Fig. 7, the thermal conductivity of the baseline and the $\text{Nd}_2\text{O}_3/\text{Yb}_2\text{O}_3$ doped coatings increased in the 800–1000 °C range. Such changes in thermal conductivity from 800 °C to 1000 °C had been observed before and were attributed to the closure of intralamellar cracks.^{5,40} However, the increase in thermal conductivity became smaller with increased dopant concentration (Table 4), suggesting that rare-earth doping reduces the effect of intralamellar crack closure on thermal conduction.

Effect of dopant type on thermal conductivity: Fig. 8 shows the thermal conductivity of coatings containing different rare-earth dopant pairs. With the thermal conductivity of YSZ plotted as a reference, it was found that the baseline had a higher thermal conductivity than the doped coatings for the measured temperature range. Among these coatings, the 7.4 mol.% (Y, Gd, Yb)₂O₃-ZrO₂ coating data exhibited the lowest thermal conductivity, and the thermal conductivities of the 7.4 mol.% (Y, Nd, Yb)₂O₃-ZrO₂ and 8.0 mol.% (Y, Nd, Gd)₂O₃-ZrO₂ coatings were comparable below 700 °C. Similar to the observation discussed above, the $\text{Gd}_2\text{O}_3/\text{Yb}_2\text{O}_3$ doped coating, which produced the most tetragonal-like XRD data over $72^\circ\text{--}76^\circ 2\theta$, exhibited the smallest thermal conductivity increase with temperature between 200 °C and 700 °C (see Table 4). Likewise, the thermal conductivity data of these coatings, regardless of dopant type pair, displayed changes corresponding to the intralamellar crack closure over 800–1000 °C. However, the thermal conductivity increase of 8.0 mol.% (Y, Nd, Gd)₂O₃-ZrO₂ was higher compared to the other two doped coatings.

Mechanisms responsible for the reduced thermal conductivity: The predominant heat transfer mode within this testing

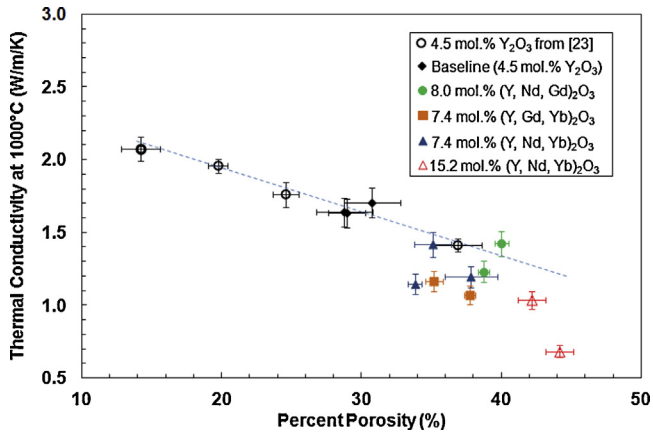


Fig. 9. Thermal conductivity values of the baseline and doped coatings taken at 1000 °C as a function of percent porosity. Additional data points obtained from *ref.* ²³ were plotted to show the effect of porosity on thermal conductivity. For a given percent porosity, the thermal conductivities of the Nd₂O₃/Yb₂O₃ and Gd₂O₃/Yb₂O₃ doped coatings are lower than that of the baseline, illustrating the effect of rare-earth doping.

temperature range is phonon conduction, and therefore, the reduced thermal conductivity observed in the doped coatings can be explained in terms of phonon scattering induced by various defects.⁴¹ While imperfections like pores, vacancies, lattice strain induced by solute atoms, and cracks shorten the mean free path of phonons and decrease the thermal conductivity, phonon scattering from grain boundaries is less important for coatings that contain grains larger than 50 nm.^{39,41,42} Determined by the intercept method, the average grain size of the baseline and the 7–8 mol.% doped coatings was found to be 230 ± 85 nm in regions close to the substrate and 799 ± 200 nm near the top. Such size variation with coating thickness was not seen in the 15.2 mol.% (Y, Nd, Yb)₂O₃-ZrO₂ coating, which has an average grain size of 194 ± 70 nm. Since the majority of grains are larger than 50 nm, contribution from grain boundaries will not be considered here.

The coatings studied in this work contained various amount of porosity, which can greatly influence the thermal conductivity of the coatings.³⁹ The orientation of pores and cracks also matters but is not considered here.⁴³ To determine the effect of porosity, the thermal conductivity measured at 1000 °C was plotted in Fig. 9 as a function of total percent porosity. In addition, the thermal conductivity data of 4.5 mol.% YSZ coatings from *ref.* ²³ were included in this figure to demonstrate further the effect of porosity on thermal conductivity. These were also SPS coatings.²³ A line to guide the eye was drawn through the conductivity data of the baseline coatings to illustrate the dependency of thermal conductivity on porosity alone. It is seen from this figure that the thermal conductivities of the doped coatings generally lie underneath the dotted line, indicating that porosity was not the only factor contributing to their lower thermal conductivities relative to the baseline coating.

The incorporation of trivalent rare-earth dopants in the zirconia lattice creates oxygen vacancies, which reduces the thermal conductivity of the doped coatings by phonon scattering. However, the variation in thermal conductivity of coatings containing

different dopant pairs was not due to the change in vacancy content since they contained a similar amount of trivalent stabilizers. Additionally, a limit exists in the yttria-zirconia system beyond which the thermal conductivity changes little with vacancy concentration.³⁹ Based on experimental results, Clarke et al.⁴⁴ concluded that, due to vacancy clustering, doping more than 8 mol.% of trivalent yttria is ineffective in further lowering the thermal conductivity. Therefore, the reduced thermal conductivity observed in the 15.2 mol.% (Y, Nd, Yb)₂O₃-ZrO₂ coating, relative to the other doped coatings, must likewise be related to scattering mechanisms other than oxygen vacancies.

Because they are larger than Zr⁴⁺ ions, Gd³⁺, Nd³⁺, and Yb³⁺ dopant ions are expected to generate strain fields in the zirconia lattice that can scatter phonons. Lattice distortion has been reported by Zhu et al.¹¹ in regions rich in rare-earth dopants. However, a comparison of dopant size shown in Table 2 and Fig. 8 suggests the degree of distortion does not scale directly with dopant ion radius. The 8 mol.% (Y, Nd, Gd)₂O₃-ZrO₂ coating contained the dopant ion pair with the two largest radii, but the thermal conductivity of this coating was higher than that of the 7.4 mol.% (Y, Gd, Yb)₂O₃-ZrO₂ coating which contained the two smallest dopant ions and less total porosity. The thermal conductivity of 7.4 mol.% (Y, Nd, Yb)₂O₃-ZrO₂ coating was comparable to that of the 8 mol.% (Y, Nd, Gd)₂O₃-ZrO₂ coating, but the former contained less total porosity, indicating that the phonon scattering induced by the Nd₂O₃/Yb₂O₃ dopant pair was more effective. This observation, consistent with the finding of Zhu and Miller⁹, suggests that the incorporation of one larger and one smaller rare-earth ion with respect to Y³⁺ can result in larger lattice disruptions and thereby decrease the thermal conductivity more effectively.

In addition to optimal dopant pairs, an optimal doping concentration may also exist. This phenomenon can be seen by comparing the thermal conductivity data in Fig. 7 for the 7.4 mol.% (Y, Nd, Yb)₂O₃-ZrO₂ and 15.2 mol.% (Y, Nd, Yb)₂O₃-ZrO₂ coatings, respectively. These data show that increasing the dopant concentration by ~3.9 times produced only a 30–35% decrease in corresponding thermal conductivity measurements. Zhu and Miller¹⁰ also noted that coatings with 10 mol.% of total dopants exhibited lower thermal conductivity than coatings containing higher dopant concentrations and suggested that this amount of dopant possibly provides the largest disruption in the zirconia lattice. These results suggest that the decrease in thermal conductivity of the 15.2 mol.% (Y, Nd, Yb)₂O₃-ZrO₂ relative to other doped coatings is partially due to increase in phonon scattering from lattice strain.

In summary, based upon the above data, the reduction in thermal conductivity observed in this study with the addition of rare-earth dopants to a 4.5 mol.% Y₂O₃-ZrO₂ powder via the SPS process was attributed primarily to the generation of porosity within the microstructure and lattice strains within the atomic structure of the resultant coatings. The 15.2 mol.% (Y, Nd, Yb)₂O₃-ZrO₂ coating had the lowest thermal conductivity but the highest % porosity, which is expected to reduce the coating modulus and therefore may not be the preferred structure and dopant concentration.

4. Conclusions

In the current work, SPS was demonstrated to be an efficient method for fabricating coatings with various rare-earth concentrations. Using SPS, coatings containing different amounts of rare-earth dopants and dopant pair types were produced. The effects of rare-earth doping on crystal structure, microstructure, and thermal conductivity of the coatings were studied. The 15.2 mol.% (Y, Nd, Yb)₂O₃-ZrO₂ coating appeared to be composed of primarily a single cubic phase; whereas, the XRD results of coatings with 7–8 mol.% of rare-earth dopants showed the potential a mixture of cubic and tetragonal or two cubic phases. In all cases, the addition of rare-earth dopants was found to also expand the interplanar spacing of the zirconia lattice. The extent of lattice expansion was determined to increase with dopant concentration and the average radii of the dopant ions. All of the coatings displayed a cauliflower structure that contained inter-columnar porosity and inter-pass boundaries. The fraction of porosity was observed to increase with dopant concentration as a result of depositing more partially melted powders, and potential mechanisms responsible for the production of these powders were discussed. The thermal conductivity of the rare-earth doped coatings was lower than that of the baseline coating. Increasing the total dopant concentration decreased the thermal conductivity by inducing additional porosity and lattice strain in the coating. Although the effect of dopant pair type on thermal conductivity was not as significant as increasing the dopant concentration, Gd₂O₃/Yb₂O₃ has been shown to be the most effective dopant pair to reduce the thermal conductivity followed by Nd₂O₃/Yb₂O₃ pair.

Acknowledgements

This work was made possible by the National Science Foundation Grant CMMI-0853297 and the support of program manager Mary Toney. The authors would like to thank Todd Snyder from Progressive Surface, MI for his help to fabricate the coatings. Part of this research was conducted through the Oak Ridge National Laboratory's High Temperature Materials Laboratory User Program, which is sponsored by the U.S. Department of Energy, Office of Energy Efficiency and Renewable Energy, Vehicle Technologies Program.

References

- Padture NP, Gell M, Jordan EH. Thermal barrier coatings for gas-turbine engine applications. *Science* 2002;**296**(5566):280–4.
- Perepezko JH. The hotter the engine, the better. *Science* 2009;**326**(5956):1068–9.
- Miller RA. Current status of thermal barrier coatings – an overview. *Surf Coat Technol* 1987;**30**(1):1–11.
- Vaßen R, Jarligo MO, Steinke T, Mack DE, Stöver D. Overview on advanced thermal barrier coatings. *Surf Coat Technol* 2010;**205**(4):938–42.
- Trice RW, Su YJ, Mawdsley JR, Faber KT, De Arellano-López AR, Wang H, et al. Effect of heat treatment on phase stability, microstructure, and thermal conductivity of plasma-sprayed YSZ. *J Mater Sci* 2002;**37**(11):2359–65.
- Witz G, Shklover V, Steurer W, Bachegowda S, Bossmann HP. Phase evolution in yttria-stabilized zirconia thermal barrier coatings studied by

- rietveld refinement of X-ray powder diffraction patterns. *J Am Ceram Soc* 2007;**90**(9):2935–40.
- Levi CG. Emerging materials and processes for thermal barrier systems. *Curr Opin Solid State Mater Sci* 2004;**8**(1):77–91.
- Zhu D, Miller RA. Thermal conductivity and sintering behavior of advanced thermal barrier coatings. In: Lin H-T, Singh M, editors. *26th Annual conference on composites, advanced ceramics, materials, and structures: B: ceramic engineering and science proceedings, vol. 23, issue 4*. John Wiley & Sons, Inc.: Hoboken, NJ; 2008. p. 457–68.
- Zhu D, Miller RA. Low conductivity and sintering-resistant thermal barrier coatings. U.S. Patent No. 7,001,859 B2, Feb. 21, 2006.
- Zhu D, Miller RA. Development of advanced low conductivity thermal barrier coatings. *Int J Appl Ceram Technol* 2004;**1**(1):86–94.
- Zhu D, Chen YL, Miller RA. Defect clustering and nano-phase structure characterization of multi-component rare earth oxide doped zirconia–yttria thermal barrier coatings. In: Kriven WM, Lin H-T, editors. *27th Annual cocoa beach conference on advanced ceramics and composites: A: Ceramic engineering and science proceedings, vol. 24, issue 3*. Hoboken, NJ: John Wiley & Sons, Inc.; 2008. p. 525–34.
- Karthikeyan J, Berndt CC, Tikkanen J, Wang JY, King AH, Herman H. Preparation of nanophase materials by thermal spray processing of liquid precursors. *Nanostruct Mater* 1997;**9**(1–8):137–40.
- Karthikeyan J, Berndt CC, Tikkanen J, Reddy S, Herman H. Plasma spray synthesis of nanomaterial powders and deposits. *Mater Sci Eng A* 1997;**238**(2):275–86.
- Ma X, Wu F, Roth J, Gell M, Jordan EH. Low thermal conductivity thermal barrier coating deposited by the solution plasma spray process. *Surf Coat Technol* 2006;**201**(7):4447–52.
- VanEvery K, Krane MJM, Trice RW, Porter W, Wang H, Besser M, et al. In-flight alloying of nanocrystalline yttria-stabilized zirconia using suspension spray to produce ultra-low thermal conductivity thermal barriers. *Int J Appl Ceram Technol* 2011;**8**(6):1382–92.
- Chen Z, Trice RW, Besser M, Yang X, Sordelet D. Air-plasma spraying colloidal solutions of nanosized ceramic powders. *J Mater Sci* 2004;**39**(13):4171–8.
- Rebollo NR, Gandhi AS, Levi CG. Phase stability issues in emerging TBC systems. In: Opila EPH, Maruyama T, Pieraggi B, Shifler D, Wuchina E, editors. *High temperature corrosion and materials chemistry iv, vol. PV-2003-16*. The Electrochemical Society, Inc.: Pennington, NJ; 2003. p. 431–42.
- Fauchais P, Etchart-Salas R, Rat V, Coudert JF, Caron N, Wittmann-Ténèze K. Parameters controlling liquid plasma spraying: solutions, sols, or suspensions. *J Therm Spray Technol* 2008;**17**(1):31–59.
- Mauer G, Guignard A, Vaßen R, Stöver D. Process diagnostics in suspension plasma spraying. *Surf Coat Technol* 2010;**205**(4):961–6.
- Muraleedharan K, Subrahmanyam J, Bhaduri SB. Identification of t' phase in ZrO₂-7.5 wt% Y₂O₃ thermal-barrier coatings. *J Am Ceram Soc* 1988;**71**(5):C-226–7.
- Erk KA, Deschaseaux C, Trice RW. Grain-boundary grooving of plasma-sprayed yttria-stabilized zirconia thermal barrier coatings. *J Am Ceram Soc* 2006;**89**(5):1673–8.
- ASTM Standard E1461-11. *Standard test method for thermal diffusivity by the flash method*. West Conshohocken, PA: ASTM International; 2012. <http://dx.doi.org/10.1520/E1461-11> www.astm.org
- VanEvery KJ. *Development and evaluation of suspension plasma sprayed yttria stabilized zirconia coatings as thermal barriers*. West Lafayette: School of Materials Engineering, Doctor of Philosophy, Purdue University; 2009.
- ASTM Standard C 373-88. *Standard test method for water absorption, bulk density, apparent porosity, and apparent specific gravity of fired whiteware products*. West Conshohocken, PA: ASTM International; 2006. <http://dx.doi.org/10.1520/C0373-88R06> www.astm.org
- Heuer AH, Chaim R, Lanteri V. The displacive cubic → tetragonal transformation in ZrO₂ alloys. *Acta Metall* 1987;**35**(3):661–6.
- Yashima M, Sasaki S, Kakihana M, Yamaguchi Y, Arashi H, Yoshimura M. Oxygen-induced structural change of the tetragonal phase around the tetragonal-cubic phase boundary in ZrO₂-YO_{1.5} solid solutions. *Acta Crystallogr Sect B Struct Sci* 1994;**50**(6):663–72.

27. Zhu D, Nesbitt JA, McCue TR, Barrett CA, Miller RA. Furnace cyclic behavior of plasma-sprayed zirconia–yttria and multi-component rare earth oxide doped thermal barrier coatings. *Ceram Eng Sci Proc* 2002;**23**: 533–46.
28. Schulz U, Schmücker M. Microstructure of ZrO₂ thermal barrier coatings applied by EB-PVD. *Mater Sci Eng A* 2000;**276**(1–2):1–8.
29. Schulz U, Leyens C, Fritscher K, Peters M, Saruhan-Brings B, Lavigne O, et al. Some recent trends in research and technology of advanced thermal barrier coatings. *Aerospace Sci Technol* 2003;**7**(1):73–80.
30. Siebert B, Funke C, Vaßen R, Stöver D. Changes in porosity and young's modulus due to sintering of plasma sprayed thermal barrier coatings. *J Mater Process Technol* 1999;**92–93**(0):217–23.
31. Kassner H, Siegert R, Hathiramani D, Vassen R, Stoeber D. Application of suspension plasma spraying (SPS) for manufacture of ceramic coatings. *J Therm Spray Technol* 2008;**17**(1):115–23.
32. VanEvery K, Krane MM, Trice R, Wang H, Porter W, Besser M, et al. Column formation in suspension plasma-sprayed coatings and resultant thermal properties. *J Therm Spray Technol* 2011;**20**(4):817–28.
33. Gell M, Xie L, Ma X, Jordan EH, Padture NP. Highly durable thermal barrier coatings made by the solution precursor plasma spray process. *Surf Coat Technol* 2004;**177–178**:97–102.
34. Fauchais P, Montavon G. Latest developments in suspension and liquid precursor thermal spraying. *J Therm Spray Technol* 2010;**19**(1–2):226–39.
35. Rampon R, Marchand O, Filiatre C, Bertrand G. Influence of suspension characteristics on coatings microstructure obtained by suspension plasma spraying. *Surf Coat Technol* 2008;**202**(18):4337–42.
36. Fazilleau J, Delbos C, Rat V, Coudert JF, Fauchais P, Pateyron B. Phenomena involved in suspension plasma spraying part 1: suspension injection and behavior. *Plasma Chem Plasma Process* 2006;**26**(4):371–91.
37. Standard thermodynamic properties of chemical substances. Haynes WM, editor. *CRC handbook of chemistry and physics, 93rd ed (internet version 2013)*. Boca Raton, FL: CRC Press/Taylor and Francis; 2013. p. 5-13–22.
38. Enthalpy of vaporization. Haynes WM, editor. *CRC handbook of chemistry and physics, 93rd ed (internet version 2013)*. Boca Raton, FL: CRC Press/Taylor and Francis; 2013. p. 6-132–7.
39. Raghavan S, Mayo MJ, Wang H, Dinwiddie RB, Porter WD. The effect of grain size, porosity and yttria content on the thermal conductivity of nanocrystalline zirconia. *Scr Mater* 1998;**39**(8):1119–25.
40. Ilavsky J, Long GG, Allen AJ, Berndt CC. Evolution of the void structure in plasma-sprayed YSZ deposits during heating. *Mater Sci Eng A* 1999;**272**(1):215–21.
41. Nicholls JR, Lawson KJ, Johnstone A, Rickerby DS. Methods to reduce the thermal conductivity of EB-PVD TBCs. *Surf Coat Technol* 2002;**151–152**:383–91.
42. Klemens PG, Gell M. Thermal conductivity of thermal barrier coatings. *Mater Sci Eng A* 1998;**245**(2):143–9.
43. Kulkarni A, Wang Z, Nakamura T, Sampath S, Goland A, Herman H, et al. Comprehensive microstructural characterization and predictive property modeling of plasma-sprayed zirconia coatings. *Acta Mater* 2003;**51**(9):2457–75.
44. Clarke DR. Materials selection guidelines for low thermal conductivity thermal barrier coatings. *Surf Coat Technol* 2003;**163–164**:67–74.